Contents lists available at ScienceDirect

Applied Catalysis B: Environmental

Evolution of oxygen vacancies in MnO_x-CeO_2 mixed oxides for soot oxidation

Lin Xueting [a], Li Shujun [a], He Hui [a], Wu Zeng [a], Wu Junliang [a], Chen Limin [a], Ye Daiqi [a,b,c], Fu Mingli [a,b,c,*]

[a] School of Environment and Energy, South China University of Technology, Guangzhou 510006, China
[b] Guangdong Provincial Key Laboratory of Atmospheric Environment and Pollution Control, Guangzhou 510006, China
[c] Guangdong Provincial Engineering and Technology Research Center for Environmental Risk Prevention and Emergency Disposal, South China University of Technology, Guangzhou 510006, China

ABSTRACT

Oxygen vacancy (O-vacancy) is essential in catalytic oxidation but little is known about its insight. Herein, a series of MnO_x-CeO_2 catalysts with various Mn/(Mn + Ce) molar ratios were synthesized with citric acid complex method for O-vacancy study in soot catalytic combustion. The samples were characterized by X-ray powder diffraction (XRD), N_2 adsorption/desorption, O_2-temperature programmed desorption (O_2-TPD), H_2-temperature programmed reduction (H_2-TPR), X-ray photoelectron spectroscopy (XPS) and in situ Raman spectroscopy. It has been shown that MnO_x(0.4)-CeO_2 catalyst presented more O-vacancies, thus exhibiting the highest catalytic activities and redox properties. With the utilization of in situ Raman, two types of O-vacancies, including Frenkel-type oxygen vacancy (F—OV) and intrinsic oxygen vacancy (I—OV), were clarified. Furthermore, the transform relation between F—OV and I—OV was found. Those two types of O-vacancies favored to the migration and transformation of active species, enhancing further the oxidation-reduction cycle and the catalytic activity for soot oxidation. In addition, Mn^{4+}/Mn^{3+}(Mn^{2+}), O_{latt}, O_{sur} and Ce^{4+}/Ce^{3+} were believed to play important roles in soot oxidation. Finally, evolution of O-vacancies was proposed, which is of significance for soot catalytic oxidation.

© 2017 Elsevier B.V. All rights reserved.

1. Introduction

Diesel engines have drawn much attention over the years owing to their fuel efficiency, reliability and durability. The widely use of diesel engines inevitably leads to an increasing amount of exhaust diesel particulate matter. Soot is one of the main toxic contaminants emitted from the diesel engine, which causes atmospheric pollution and has a deleterious effect on human health [1–3]. Therefore, efforts to reduce soot emission are an ongoing hot topic. DPF (diesel particulate filter) [4–6] is considered as the most popular and efficacious technology for soot elimination. However, their high working temperatures without catalysts (around 600 °C) [3,7] has hindered the application in soot removal at usual diesel exhaust temperature (175–400 °C) [8]. Thus, the use of oxidative catalyst to lower the combustion temperature for soot abatement is believed to be a feasible and promising method in reducing soot emission.

Ceria oxide exhibits excellent catalytic activities due to its special oxygen storage capacity (OSC), which can store and release highly active oxygen species. This property of ceria oxide makes the material exceptionally effective in catalytic applications [6,9–12]. Manganese oxide has been widely used as the catalysts in many oxidation and reduction reactions [13–15]. The high activity of manganese is ascribed to the element's multivalent oxidation states (mainly Mn^{2+}, Mn^{3+} and Mn^{4+}) and the high mobility of lattice oxygen [15,16]. Compared with pure CeO_2 and MnO_x, MnO_x-CeO_2 catalyst has showed superior or excellent activity with much lower ignition temperature owing to the synergistic effect between the bimetal oxides in the solid solution [17–20].

Many researchers have focused on studying the determining factors and clarifying the reaction mechanisms for soot oxidation. Shimizu and Makkee et al. [7,21] reported that active oxygen exerts a prominent role in soot catalytic oxidation. Wu and Shan et al. [17,18,22] revealed that the incorporation of Mn into the ceria lattice had accelerated the active oxygen mobility and promoted the

evolution of lattice oxygen favoring to soot oxidation. Machida, Hornoiu and Lopez et al. [11,23,24] found that O-vacancies formed from the moment active oxygen spilled over from the catalyst onto the soot surface, and the gaseous O_2 subsequent fulfilled the O-vacancies to re-oxidize the catalyst. Wu and S. Agarwal et al. [25,26] proposed the reliable assignments of the defect bands in Raman spectra and clarified the types of O-vacancies. Over the past years, it is generally considered that O-vacancies can significantly affect the catalytic reaction. A tremendous amount of effort had been made to understand the nature of active oxygen and O-vacancies. Our previous works also demonstrated the importance of oxygen species and O-vacancies in soot removal [27,28]. However, little is known about the insight of O-vacancies which is crucial for clarifying the reaction mechanisms. Real-time study of its evolution still needs further investigations.

In this work, in situ Raman spectroscopy, the powerful and efficient tool for analyzing redox couple and defect sites like O-vacancies, is introduced for intensive study of MnO_x-CeO_2 with the intention of elucidating the nature of O-vacancies and their relationship. Here, by using this cutting-edge tool, we follow up researches above by clarifying the roles of two different types of O-vacancies, illuminating their relationship and proposing the evolution of O-vacancies in soot oxidation over all samples. In addition, the critical factors for the superior catalytic activity and the oxidation-reduction cycle for soot catalytic combustion are discussed.

2. Experimental

2.1. Catalyst preparation

The catalysts were synthesized using citric acid complex method [29]. $Mn(CH_3COO)_2 \cdot 4H_2O$ and $Ce(CH_3COO)_3 \cdot 5H_2O$ were added in deionized water in molar ratios of Mn/(Mn + Ce) = (0, 0.1, 0.3, 0.4, 0.5, 0.6, 1) at 70 °C. The pH of the prepared Mn/(Mn + Ce) solution was adjusted to 1.5, and then the solution was stirred at 90 °C until the transparent gel formed. Then it was quickly transferred to the oil bath pan to be held at 150 °C before the materials were completely agglomerated. The resulting materials were dried at 120 °C for 2 h, after then calcinated at 550 °C for 5 h in air. Catalysts were coded as $MnO_x(z)$-CeO_2 (z = 0, 0.1, 0.3, 0.4, 0.5, 0.6, 1).

2.2. Catalyst characterization

XRD was performed on a D8 ADVANCE diffractometer (Bruker, Germany) with CuKα radiation (40 kV, 40 mA). Data were collected between 2θ = 10–90° with a step size of 0.02°.

Nitrogen adsorption/desorption isotherms were measured at 77 K on an ASAP2020 M analyzer (Micromeritics, USA). All samples were outgassed at 300 °C in vacuum for 4 h before measurement.

O_2-TPD was carried out by Auto ChemIIChemisorption Analyzer (Micromeritics, USA). A 200 mg sample was pre-treated in He at 300 °C for 30 min, then cooled down to 60 °C, and subsequently treated by 50 ml min^{-1} 5% O_2/He mixture gas for 1 h. Finally, the reactor temperature rose at a rate of 10 °C min^{-1} to 900 °C. The outlet exhaust was detected by TCD.

H_2-TPR was performed in the same apparatus as used in O_2-TPD. A 150 mg sample was pre-treated in Ar at 300 °C for 30 min. After the sample was cooled down to 60 °C, 10% H_2/Ar mixture gas was introduced and the reactor was heated at a rate of 10 °C min^{-1} to 900 °C, and the outlet exhaust was also detected by TCD. Quantification of H_2 consumption was carried out by calibrating the signal with the introduction of known amounts of hydrogen.

XPS signals were acquired on ESCALAB 250 photoelectron spectrometer (Thermo-VG Scientific,USA). Charge effects of samples were corrected by setting the binding energy of adventitious carbon (C1s) at 284.6 eV.

The Raman spectra of the catalysts were recorded in a LabRAM HR Evolution Laser Raman Spectrometer (HYJ, France) with a HeNe laser and a CDD detector. The visible Raman spectra (wave number region from 300 to 800 cm^{-1}) and the UV Raman spectra (wave number region from 300 to 1350 cm^{-1}) were collected using the exciting line at 532 cm^{-1} and 325 cm^{-1}, respectively.

In situ Raman spectra of catalyst/model soot (Printex®U, Degussa) mixture: 30 mg of soot and 270 mg of catalyst were mixed carefully by an agate mortar for 2 min for "loose contact" conditions. Then samples were heated from 30 °C to 500 °C then back to 30 °C under Ar or O_2(10%) + Ar(balance) atmospheres in an in-situ reaction tank. And the spectra were achieved at every 100 °C. Temperature programme: ramping rate 10 °C min^{-1}; cooling rate 20 °C min^{-1}.

2.3. Catalytic activity evaluation

The catalytic activity was evaluated by a temperature programmed oxidation (TPO) apparatus in 10% O_2/Ar with a total flow
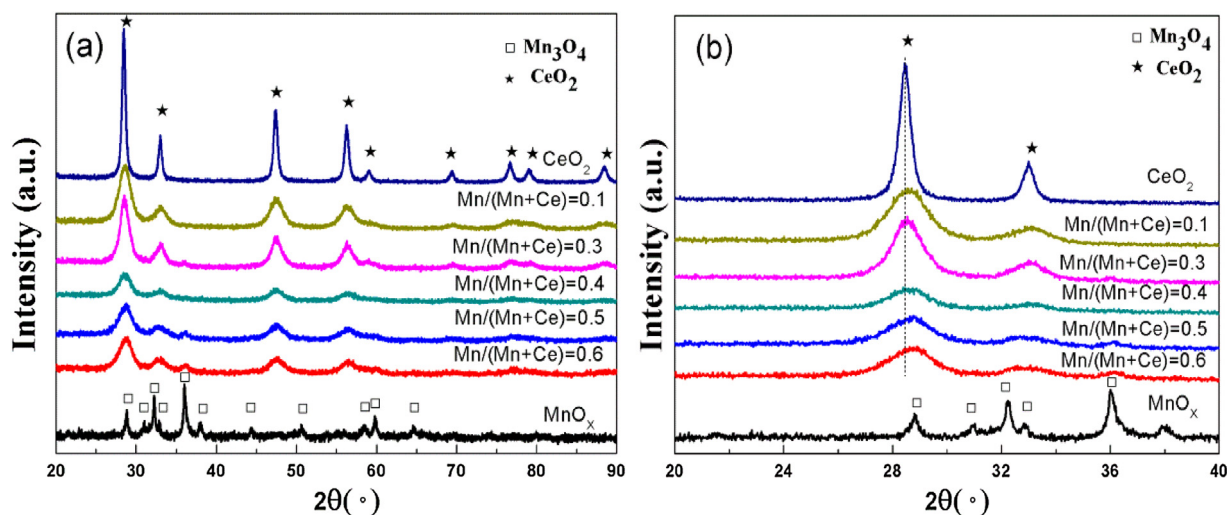

Fig. 1. (a)XRD profiles of $MnO_x(z)$-CeO_2 catalysts. (b) spectra at the range of 20°-40° from (a).

Table 1
Specific surface area, average crystallite size and lattice parameter of $MnO_x(z)$-CeO_2 catalysts.

Catalyst	SSA[a]/(m² g⁻¹)	d [b](nm)	Lattice parameter (nm)
CeO_2	15.8	16.10	0.5402
$MnO_x(0.1)$-CeO_2	107.8	5.25	0.5385
$MnO_x(0.3)$-CeO_2	90.9	6.33	0.5399
$MnO_x(0.4)$-CeO_2	125.2	4.87	0.5375
$MnO_x(0.5)$-CeO_2	113.7	5.06	0.5381
$MnO_x(0.6)$-CeO_2	104.4	4.91	0.5389
MnO_x	5.7	24.06	–

[a] specific surface area.
[b] average crystallite size.

rate of 100 ml min⁻¹. Before catalytic activity evaluation, 30 mg of soot (Printex® U, Degussa) and 270 mg of catalyst were also mixed carefully by an agate mortar for 2 min for "loose contact" conditions. In order to prevent reaction runaway, 300 mg of the soot-catalyst mixture was diluted with 900 mg of silica, then the diluted mixture was placed in a tubular quartz reactor (I.D.=12 mm,O.D.=16 mm). The oxidation test was carried out in the temperature range from RT to 650 °C. The outlet CO_2 was monitored using a KC GC-900A (China) equipped with TCD and TDX-01 [29]. As no obvious CO product was observed during the catalytic activity evaluation, the CO_2 data were only used to present the catalytic activity for the catalytic soot combustion. T_i was the ignition temperature when the CO_2 concentration in the outlet exhaust reached 5000×10^{-6} (5000 ppm) for the first time [18,30]. T_m represented the temperature of the maximum CO_2 concentration [29]. For comparison convenience, the temperature at which the CO_2 concentration in the outlet gas declined to 1000 ppm was referred to as the burnout temperature (T_c) of soot oxidation, and the burning interval ΔT was defined as $T_c - T_i$.

3. Results and discussion

3.1. Characterization

3.1.1. Textural and structural characterization

The structure of catalysts was studied by XRD measurement. The XRD patterns are shown in Fig. 1, and the calculated average crystallite size and lattice cell parameters [9,30–32] are listed in Table 1. Fig. 1 shows that all diffraction peaks of MnO_x can be ascribed to Mn_3O_4 (JCPDS 18-0803). And all reflections of CeO_2 are attributed to cubic fluorite structure (JCPDS 34-0394) [17]. The broad characteristic peaks of $MnO_x(z)$-CeO_2 are similar to that of the single CeO_2 [33]. With increasing Mn-incorporating content, the (111) diffraction peaks shift toward higher diffraction angle and the intensities become weaker (Fig. 1b). In addition, the lattice parameter of $MnO_x(z)$-CeO_2 (Table 1) decreases slightly compared with that of pure CeO_2, which may be due to the replacement of Ce^{n+} by Mn^{n+}. This is consistent with the result that part of Mn species enter into the ceria lattice and provoke the contraction of its unit cell [17,19,34]. Besides, the average crystallite size were calculated using Scherrer's equation. And the BET surface areas measured by N_2 adsorption/desorption are listed in Table 1. Based on the data, it can be easily found that $MnO_x(z)$-CeO_2 exhibits much smaller crystallite size than MnO_x and CeO_2. And the BET surface area of $MnO_x(z)$-CeO_2 is sharply increased with respect to that of single CeO_2. The results demonstrate evidence for the fact that incorporation of Mn would limit the growth of ceria crystallites and result in an increase in SSA. On the basis of above findings, it can be concluded that MnO_x is incorporated into ceria lattice to form Mn-Ce solid solution.
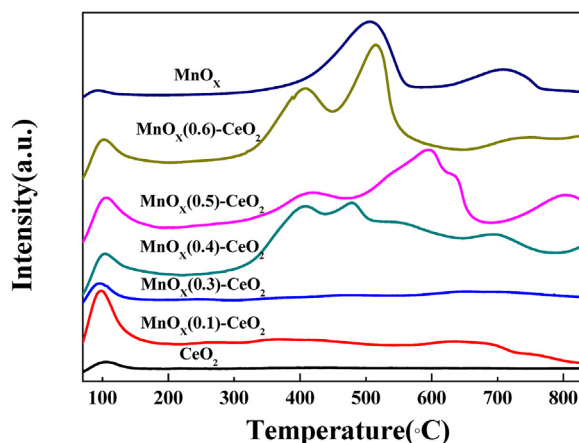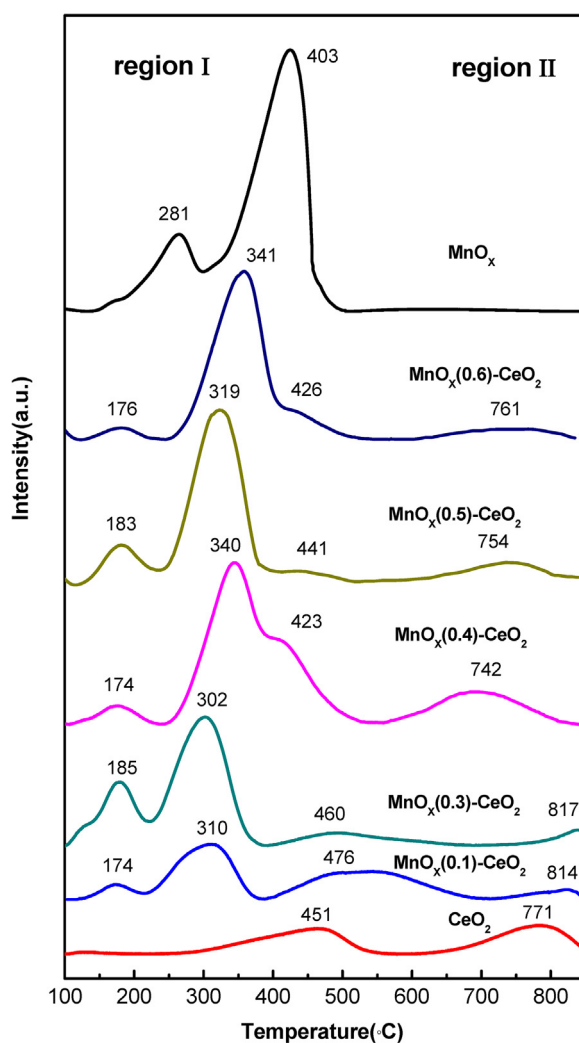

Fig. 2. O_2-TPD profiles of $MnO_x(z)$-CeO_2 catalysts.

Fig. 3. H_2-TPR profiles of $MnO_x(z)$-CeO_2 catalysts.

3.1.2. O_2 desorption behavior

O_2-TPD had been used for studying oxygen species and oxygen desorption behavior. The results are shown in Fig. 2. Two kinds of peaks are presented in the spectra. Firstly, test on single CeO_2 shows one minor peak at 107 °C, which is due to desorbed α-oxygen ion from molecular O_2, O_2^- and O_2^{2-} adsorbed on O-vacancies [18]. It should be noted that the formation of α-oxygen species is due to

Table 2
H_2 consumption for various samples.

Sample	Peak position (°C)	H_2 consumption[a] (μmol g_{cat}^{-1})	Total H_2 consumption[b] (μmol g_{cat}^{-1})
CeO_2	451, 771	–	102.3
$MnO_x(0.1)$-CeO_2	174, 310, 476	110.9	112.1
$MnO_x(0.3)$-CeO_2	185, 302, 460	121.3	124.6
$MnO_x(0.4)$-CeO_2	174, 340, 423	137.4	158.3
$MnO_x(0.5)$-CeO_2	183, 319, 441	130.1	141.2
$MnO_x(0.6)$-CeO_2	176, 341, 426	128.2	136.3

[a] H_2 consumed from the three low-temperature peaks.
[b] Overall H_2 consumption in H_2-TPR.

adsorption of O_2 at anion vacancy, and they can be easily desorbed at low temperature [35]. For $MnO_x(z)$-CeO_2, similar desorption peaks appear in the range of 70–200 °C, but with small shifts toward lower temperature and are slightly stronger. The results lead to the conclusion that desorption of α-oxygen for the catalysts is significantly enhanced via dissolute MnO_x into the ceria lattice. Secondly, another peak in the range of 300–780 °C is ascribed to β-oxygen desorbed from the liberation of lattice oxygen [36]. The β-oxygen in the surface lattice can be desorbed at a temperature about 400 °C along with the reduction of Mn^{4+} to Mn^{3+} and the generation of O-vacancy [37]. The β-oxygen desorption process continues via the diffusion of lattice oxygen from the bulk to the surface and the further reduction of Mn^{3+} to Mn^{2+} and Ce^{4+} to Ce^{3+} [36]. It can be observed that $MnO_x(z)$-CeO_2 shows lower desorption temperature and stronger intensity compared with single ceria and MnO_x, indicating that both the oxygen desorption capacity and the mobility of lattice oxygen are improved in the mixed oxides.

3.1.3. Catalysts reducibility

The H_2-TPR test was applied for studying redox property of the samples (Fig. 3). Two reduction peaks of CeO_2 are detected at 473 °C and 795 °C. The 473 °C peak can be attributed to the surface CeO_2 being reduced to Ce_2O_3, while the 795 °C peak is due to the same reduction process in the bulk of the catalyst [38,39]. Another two strong reduction peaks can also be found in the curve of MnO_x at 281 °C and 403 °C, respectively, which are related to the reduction of Mn oxides crystallites ($MnO_2/Mn_2O_3 \rightarrow Mn_3O_4 \rightarrow MnO$) [3,15,17]. H_2-TPR analysis of $MnO_x(z)$-CeO_2 shows four peaks approximately at 180 °C, 340 °C, 410 °C and 780 °C, respectively. The first two reduction peaks below 400 °C (region I) are ascribed to the $Mn^{4+}/Mn^{3+}(Mn^{2+})$ reduction, while the other two overlapped peaks between 400 °C and 850 °C (region II) should be ascribed to the reduction of Ce^{4+} to Ce^{3+}, where 400 °C for the reduction on surface and 850 °C in the bulk of the solid solutions [17]. Fig. 3 shows that the reduction peaks of $MnO_x(z)$-CeO_2 shift to lower temperature compared with that of single MnO_x or CeO_2. This indicates that the incorporation of Mn into CeO_2 promotes the redox properties thereby exhibiting low temperature reduction patterns. And this is generally believed to be associated with highly mobilized oxygen species, explaining the rapid generation of active sites on the surface for the H_2 adsorption [40]. Additionally, for $MnO_x(z)$-CeO_2, the reduction peak areas are strongly enhanced with the increasing Mn-incorporating amount, especially in the range of 100–600 °C. The consumption of hydrogen is calculated and displayed in Table 2. $MnO_x(0.4)$-CeO_2 exhibits the largest peak areas or maximum OSC.

3.2. Catalytic activity

Fig. 4 shows the TPO patterns of catalytic combustion of soot on the CeO_2, $MnO_x(z)$-CeO_2 and MnO_x in 10%O_2/Ar. T_i, T_m, T_c and ΔT are summarized in Table 3. It is showed that T_i over the single CeO_2 and MnO_x decreases to 349.5 °C and 357.3 °C respectively, compared with 457.0 °C without catalyst. For the $MnO_x(z)$-CeO_2 catalysts, T_i varied between 254.5 °C
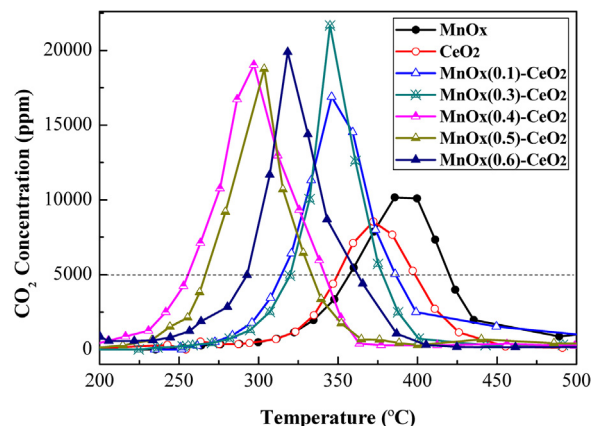
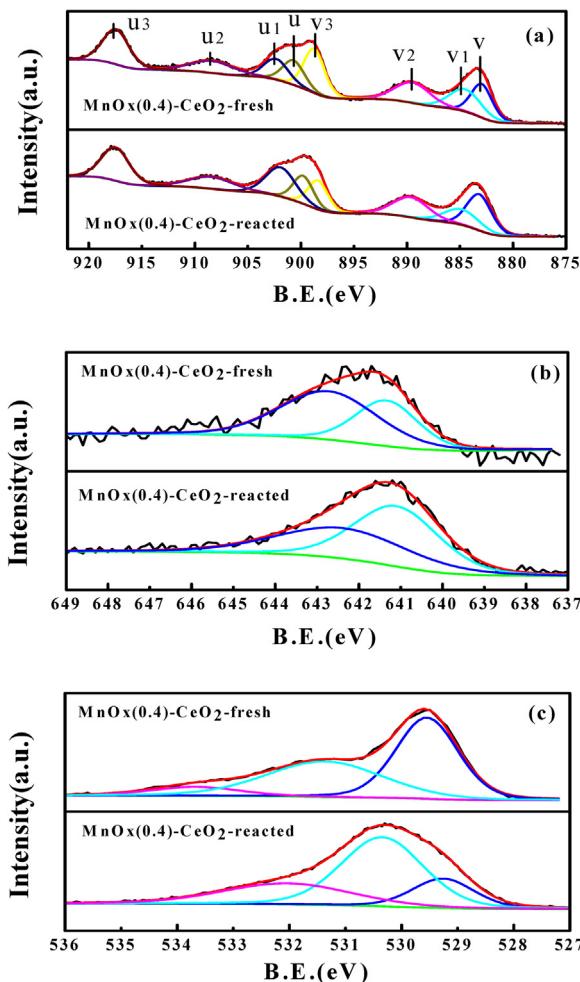**Fig. 4.** TPO profiles for soot oxidation over $MnO_x(z)$-CeO_2.

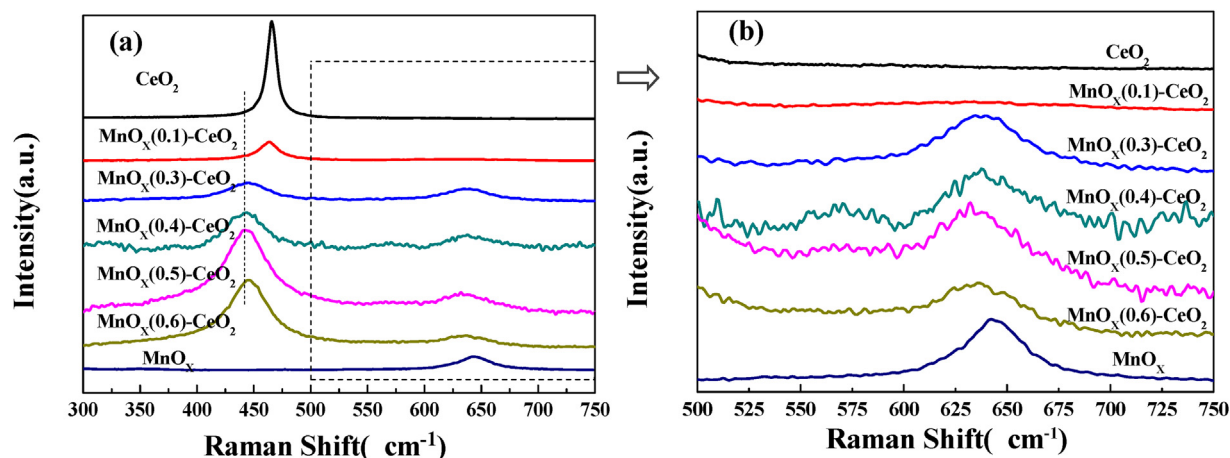**Fig. 5.** XPS spectra of Ce3d(a), Mn2p(b) and O1s(c) for $MnO_x(0.4)$-CeO_2.

Fig. 6. (a)Visible Raman spectra of $MnO_x(z)$-CeO_2 catalysts; (b)spectra in black-dotted box from (a).

Table 3
T_i,T_m,T_c and ΔT for soot combustion on $MnO_x(z)$-CeO_2 catalysts.

Catalyst	$T_i{}^a$/$^\circ$C	$T_m{}^b$/$^\circ$C	$T_c{}^c$/$^\circ$C	$\triangle T^d$/$^\circ$C
Noncatalyst	457.0	550.0	642.0	185.0
CeO_2	349.5	372.2	430.9	81.4
$MnO_x(0.1)$-CeO_2	314.2	346.0	499.6	185.4
$MnO_x(0.3)$-CeO_2	319.8	344.9	399.1	73.3
$MnO_x(0.4)$-CeO_2	254.5	299.0	359.4	101.9
$MnO_x(0.5)$-CeO_2	267.7	303.6	357.9	90.2
$MnO_x(0.6)$-CeO_2	293.0	318.4	387.9	94.9
MnO_x	357.3	385.7	481.8	124.5

[a] the ignition temperature when the CO_2 concentration in the outlet exhaust reached 5000×10^{-6} (5000 ppm) for the first time.
[b] the temperature of the maximum CO_2 concentration.
[c] the burnout temperature of soot oxidation (the CO_2 concentration in the outlet gas declined to1000 ppm).
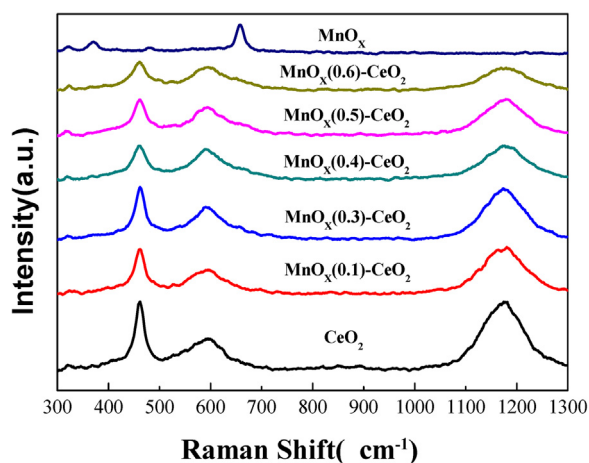[d] the burning interval ($T_c - T_i$).
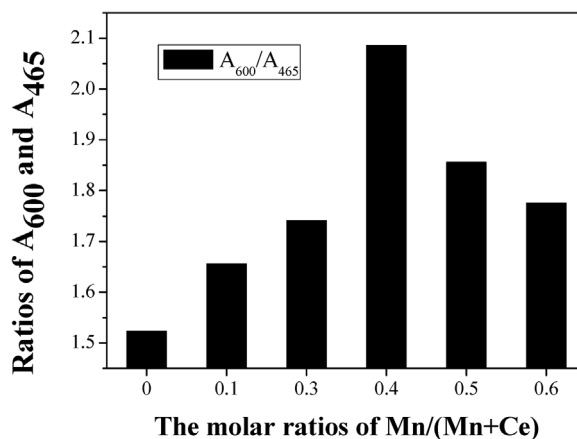

Fig. 7. UV Raman spectra of $MnO_x(z)$-CeO_2 catalysts.

Fig. 8. The concentration of surface oxygen vacancies with different molar ratios of $MnO_x(z)$-CeO_2 catalysts.

and 319.8 °C, which is about 29.7-95.0 °C lower than that over the single CeO_2 (T_i = 349.5 °C). Therefore, the combination of CeO_2 and MnO_x seems to possess further improvement on the soot oxidation activity. Soot oxidation activity decreases in the following order: $MnO_x(0.4)$-CeO_2 > $MnO_x(0.5)$-CeO_2 > $MnO_x(0.6)$-CeO_2 > $MnO_x(0.3)$-CeO_2 > $MnO_x(0.1)$-CeO_2 > CeO_2 > MnO_x. It is noticeable that $MnO_x(0.4)$-CeO_2 exhibits the highest activity for soot oxidation with T_i of 254.5 °C, remarkably lower than 457.0 °C in the case of noncatalyst reaction. This is in accordance with the lowest O_2-desorption temperature and maximum OSC for $MnO_x(0.4)$-CeO_2, as detected by O_2-TPD and H_2-TPR. Additionally, it is noted that the areas under the peaks for MnO_x and CeO_2 in the TPO profiles obviously smaller than those for $MnO_x(z)$-CeO_2, indicating the formation of more C—O intermediate species when using pure catalyst during soot oxidation process.

3.3. Xps

To further investigate the surface chemical states and the types of oxygen species during reaction, the fresh and reacted $MnO_x(0.4)$-CeO_2 (best redox property) were chosen to be analyzed by XPS

Table 4
Atomic ratios by XPS surface compositional analysis for $MnO_x(0.4)$-CeO_2.

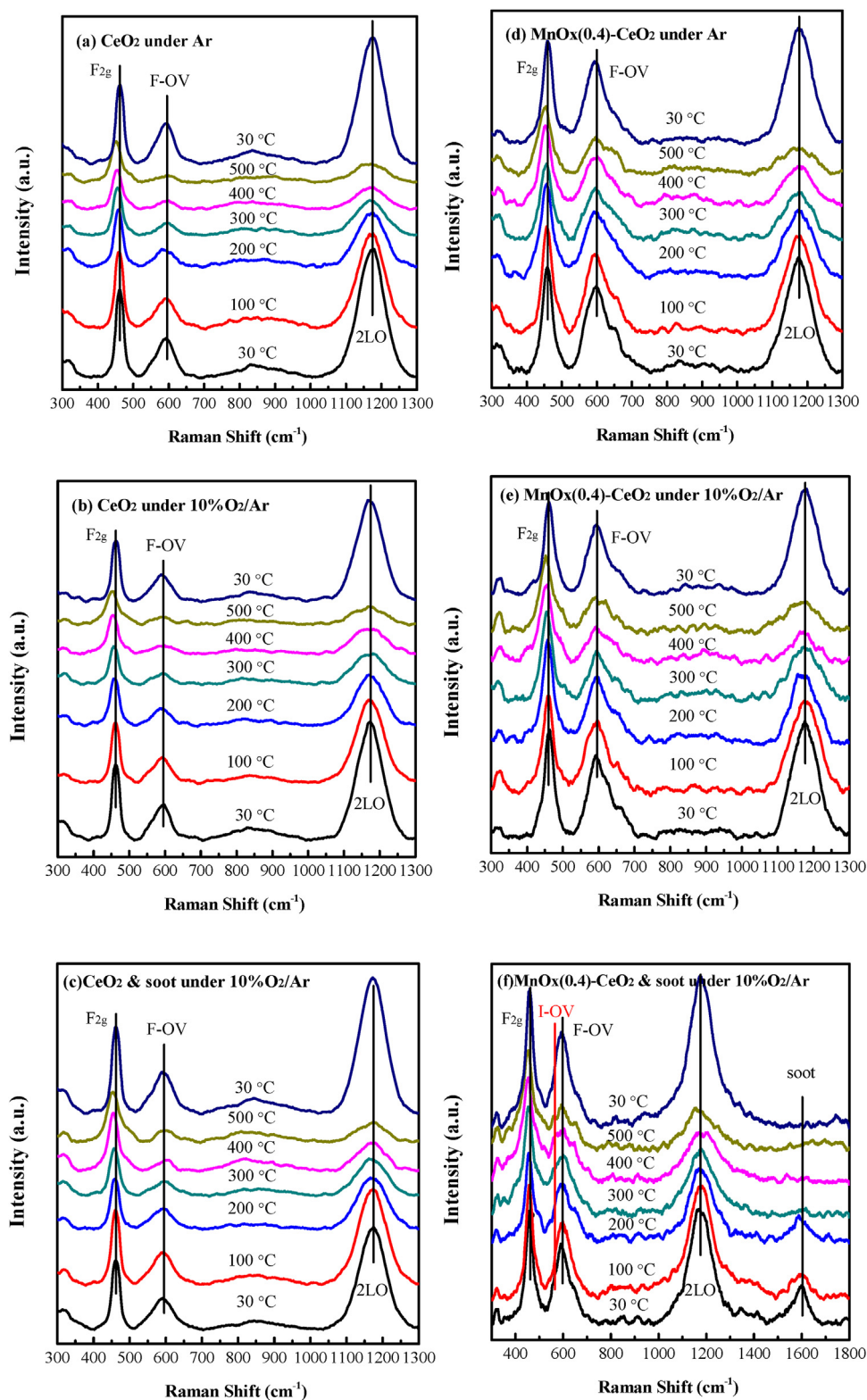| Sample	O/(at.%)			Ce^{4+}/Ce^{3+}	Mn^{4+}/$(Mn^{2+} + Mn^{3+})$
	O_{ads}	O_{sur}	O_{latt}		
$MnO_x(0.4)$-CeO_2-fresh	8.0	41.5	50.5	4.47	1.75
$MnO_x(0.4)$-CeO_2-reacted	26.5	55.6	17.9	4.05	0.78

Fig. 9. In situ UV Raman spectra of (a,b,c) CeO_2 and (d,e,f) $MnO_x(0.4)$-CeO_2 under (a,d) Ar, (b,e) $10\%O_2$/Ar and (c,f) reactants (soot and $10\%O_2$/Ar). Temperature programme: ramping rate of $10\,°C\,min^{-1}$ from 30 to $500\,°C$ and $20\,°C\,min^{-1}$ from 500 to $30\,°C$.

(Fig. 5). Table 4 lists the surface atomic ratios of $MnO_x(0.4)$-CeO_2. In the Ce 3d spectra, the label u and v peaks belong to the $3d_{3/2}$ and $3d_{5/2}$ spin orbit component, respectively. The dominant peaks denoted by v, v_2, v_3, u, u_2 and u_3 are characteristic peaks of Ce^{4+}, whereas the peaks marked by v_1 and u_1 represent those of Ce^{3+} [41,42]. As can be noted in the table, the Ce^{4+}/Ce^{3+} ratios on the

fresh and reacted catalyst are 4.47 and 4.05 (>1), respectively, suggesting that Ce is mostly in a +4 oxidation state. In the Mn 2p spectra, the binding energy values around 642.6 eV and 641.3 eV are characteristic of Mn^{4+} and Mn^{3+} (or Mn^{2+}) species, respectively [43]. The corresponding O1s spectra of $MnO_x(z)$-CeO_2 possess three peaks: lattice oxygen (O_{latt}) at ~529–530 eV, surface oxygen (O_{sur})
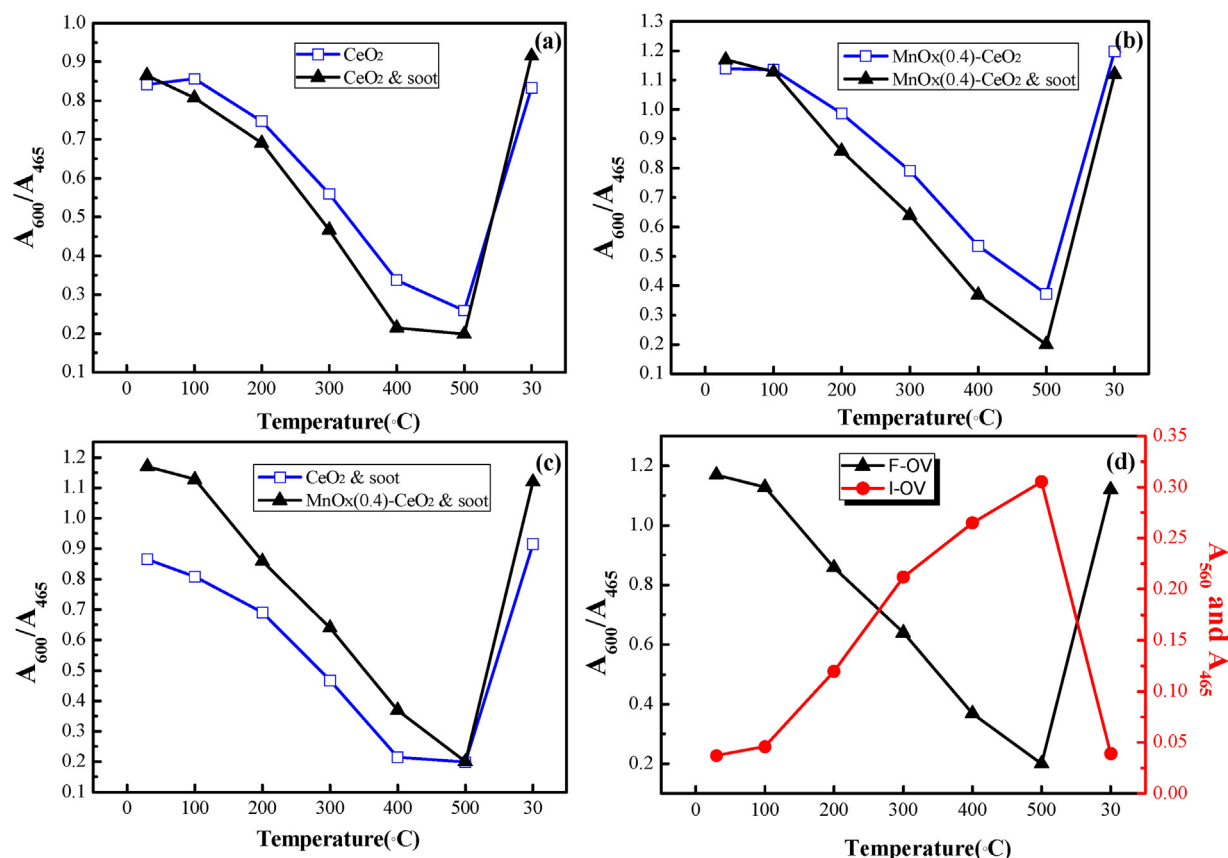
Fig. 10. (a,b,c)Peak intensity ratio of A_{600}/A_{465} as a function of the temperature for CeO_2 and $MnO_x(0.4)$-CeO_2 under $10\%O_2/Ar$ and reactants (soot and $10\%O_2/Ar$). (d)Peak intensity ratio of A_{560}/A_{465} and A_{600}/A_{465} from spectra of $MnO_x(0.4)$-CeO_2 under reactants (soot and $10\%O_2/Ar$). The peak intensity values were taken from Fig. 9.

at ~530–532 eV assigned to defect oxide or the surface oxygen ions, and adsorbed oxygen species (O_{ads}) at ~533–534 eV [44,45]. Table 4 shows that the ratio of $Mn^{4+}/(Mn^{3+}+Mn^{2+})$ for reacted catalyst decreases notably, accompanied by a slight decrease of Ce^{4+}/Ce^{3+}, providing proves in terms of their participation in redox cycle. As for oxygen species, O_{latt} declines remarkably after reaction, while O_{sur} shows an increase. In addition, O_{ads} on the catalyst also increases after reaction, which may be due to the gas phase O_2 adsorb onto the surface O-vacancy to replenish the active oxygen, causing by continuous consumption of O_{sur} and O_{latt} species during soot oxidation process [46]. In general, the amount variations of Mn, O and Ce species suggest that mixed oxides catalyze soot oxidation with the participation of $Mn^{4+}/Mn^{3+}(Mn^{2+})$, O_{latt}, O_{sur} and Ce^{4+}/Ce^{3+}. Identical conclusion can also be made from XPS results (Table S1) of other samples $MnO_x(z)$-$CeO_2(z = 0.1, 0.3, 0.5, 0.6)$. Moreover, Machida et al. [23]. had revealed that the reactivity of oxygen species involved in the redox cycle were critical to soot oxidation. Therefore, this XPS characterization gives great support to elucidate the soot catalytic oxidation.

3.4. Visible and UV Raman

In order to probe the insights of catalytic activity over $MnO_x(z)$-CeO_2 catalysts, Raman spectroscopy is introduced. It is generally believed that active species, including O-vacancies and defect sites, are of great importance in influencing the surface reactivity by modifying the local electronic structure [47–49]. Therefore, Raman spectroscopy, as a powerful characterization technique for detecting O-vacancies, is employed to investigate the unsolved nature of O-vacancies and their evolution.

Fig. 6 shows the visible Raman results of CeO_2, $MnO_x(z)$-CeO_2 and MnO_x catalysts. A Raman characteristic band at ca. 465 cm^{-1} is detected in pure CeO_2, which can be safely assigned as the oxygen breathing frequency around the Ce^{4+} ions (F_{2g} mode) [17,31]. And the band observed around ca. 650 cm^{-1} is attributed to separated phases of Mn_3O_4. Therefore, it can be clearly concluded that the incorporation of Mn into ceria indeed leads to the formation of solid solution, which is consistent with the XRD result. However, the Raman bands at 465 cm^{-1} over $MnO_x(z)$-CeO_2 increase in bandwidth, together with small down-shifts. The broadening of these bands is a size-dependent phenomenon, which is caused by the inhomogeneous strain broadening associated with dispersion in particle size and by phonon confinement [25]. And as the Raman technique is a surface characterization technique, down-shifts of these band are correlated to the surface O-vacancies [38].

As is widely known that compared to visible Raman, UV Raman has the advantage in terms of probing defect sites, which can be explained by the resonance Raman effect [50,51]. Fig. 7 shows the UV Raman of CeO_2, $MnO_x(z)$-CeO_2 and MnO_x catalysts. Two new bands appear when UV laser is applied. The band around 600 cm^{-1} is attributed to the defect sites (O-vacancies) and around 1179 cm^{-1} to second-order longitudinal optical (2LO) mode [25]. Here, to get a better look at the O-vacancies, we listed the ratios of integral intensity (A_{600}/A_{465}) over $MnO_x(z)$-CeO_2 in Fig. 8. It can reflect the relative O-vacancy concentration [50]. The relative intensity ratio is thus in the order $MnO_x(0.4)$-$CeO_2 > MnO_x(0.5)$-$CeO_2 > MnO_x(0.6)$-$CeO_2 > MnO_x(0.3)$-$CeO_2 > MnO_x(0.1)$-$CeO_2 > CeO_2 > MnO_x$, which agrees well with the TPO results. This result is reasonably, since it has been well established that O-vacancies can closely impact catalytic reaction. As expected, $MnO_x(0.4)$-CeO_2 can offer more O-vacancies, which is in good agreement with its largest oxygen

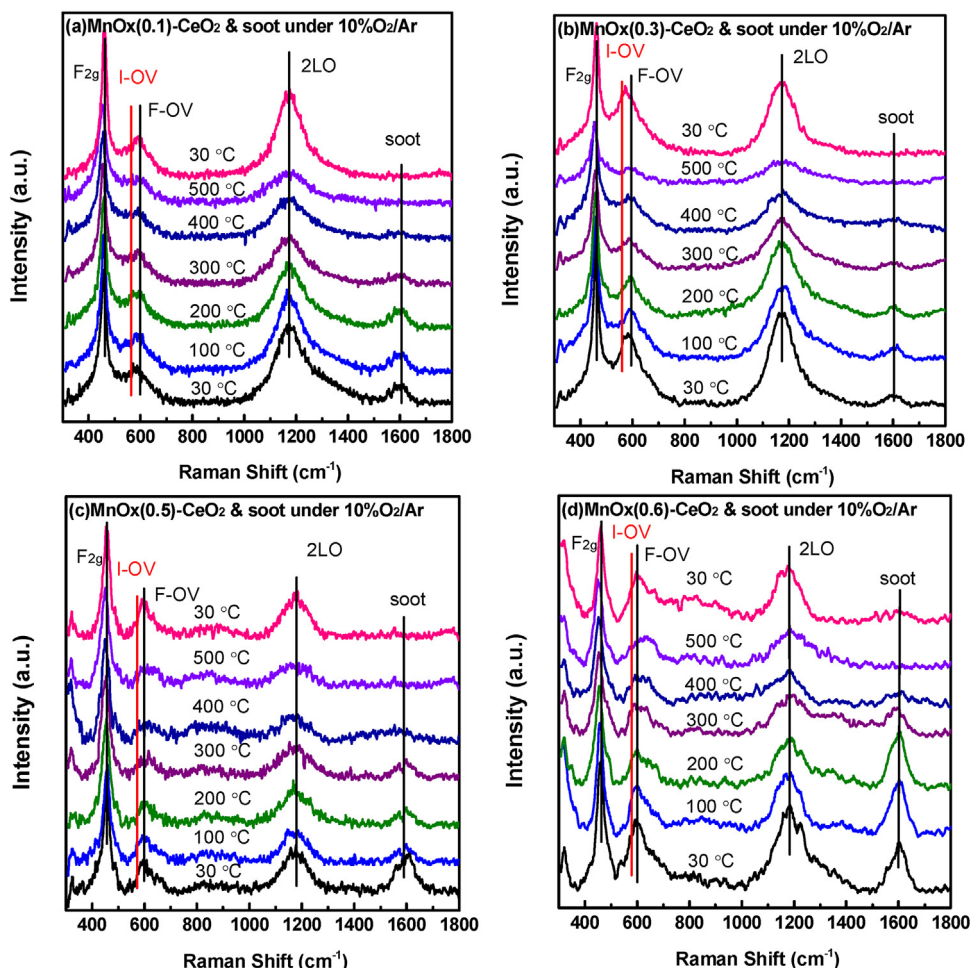**Fig. 11.** In situ UV Raman spectra of (a)MnOx(0.1)-CeO$_2$, (b)MnOx(0.3)-CeO$_2$, (c)MnOx(0.5)-CeO$_2$ and (d)MnOx(0.6)-CeO$_2$ under reactants (soot and 10%O$_2$/Ar). Temperature programme: ramping rate of 10 °C min^{-1} from 30 to 500 °C and 20 °C min^{-1} from 500 to 30 °C.

desorption capacity, as proved by O$_2$-TPD test. This indicates that appropriate amount of Mn incorporating into the ceria lattice can deform the structure and subsequently conduce to formation of O-vacancies [22], thus leading to the highest catalytic activity.

For the purpose of observing evolution of O-vacancies during soot combustion, in situ Raman was conducted in an in-situ reaction tank under different atmospheres. MnO$_x$(0.4)-CeO$_2$, as the most active catalyst, was tested. In situ UV Raman spectra of CeO$_2$ and MnO$_x$(0.4)-CeO$_2$ were recorded under Ar (Fig. 9a,d), 10%O$_2$/Ar (Fig. 9b,e) and reactants (soot and 10%O$_2$/Ar; Fig. 9c,f) in a temperature range of 30–500 °C. As the temperature goes up, down-shifts and increase in bandwidth of the 465 cm^{-1} band are observed, suggesting a mild growth in grain size [52]. However, the shape of the band recovers when temperature drops back to 30 °C, suggesting that lattice thermal expansion in CeO$_2$ is reversible.

For the defect band at 600 cm^{-1}, the assignment is still controversial. According to several studies regarding to this controversy in the past years [50,53–56], there are three types of defects that are considered to be the reasons of the 600 cm^{-1} band, including MO8-type defect structure, I—OV and F—OV. First of all, it can be easily ruled out the option of MO8-type defect structure. Because the formation of this structure may need another ions (denoted as M^{4+}) with different radii to dope into CeO$_2$. However, the 600 cm^{-1} band is clearly observed in pure CeO$_2$ samples (Fig. 9a–c), suggesting the defect band is not caused by doping of M^{4+}. Secondly, intrinsic defect sites can actively absorb gas O$_2$, meaning that intrinsic defect band should not exist upon introduction of 10%O$_2$/Ar,

which can not correspond to the observations of 600 cm^{-1} band in Fig. 9(b,c,e,f). Thus we prefer the assignment of the defect band at 600 cm^{-1} as the Frenkel-type oxygen vacancy in CeO$_2$. The formation of F—OV in CeO$_2$ lattice is caused by some oxygen anions escaping from the original tetrahedral sites to the octahedral sites [25], resulting in the lattice oxygen turning into interstitial oxygen. Meanwhile, O-vacancies form. In the case of MnO$_x$(0.4)-CeO$_2$, when Ce^{4+} ions are substituted by Mn^{4+}, relocations of some oxygen anions occur. Thus, the F—OV subsequently form. Clearly this assignment can well explain the appearance of the 600 cm^{-1} band under 10%O$_2$/Ar because the O-vacancies are charge-balanced by the interstitial oxygen in the octahedral sites so that they are not able to adsorb extra oxygen [25]. Also, it is worth noting that decrease of the 600 cm^{-1} band intensity occurs as the temperature rises and then recovers when the temperature drops back to 30 °C, showing that the interstitial oxygens are mobilized in CeO$_2$ lattice.

When comparing the Raman spectra between CeO$_2$ and MnO$_x$(0.4)-CeO$_2$, a shoulder band at 560 cm^{-1} (Fig. 9f), which has been ascribed to intrinsic defect band [26], is observed at 200 °C. The reason for the formation of intrinsic defect sites is different from the Frenkel-type oxygen defects. It is caused by the escape of interstitial oxygen from the lattice, thus leaving O-vacancies in original sites. The unstable interstitial oxygen is readily to escape to surface, exhibiting highly mobilized property, thus facilitating the rapid and repeatable redox cycles. Also, previous studies [26,57] have demonstrated that I—OV can form and disappear due to the
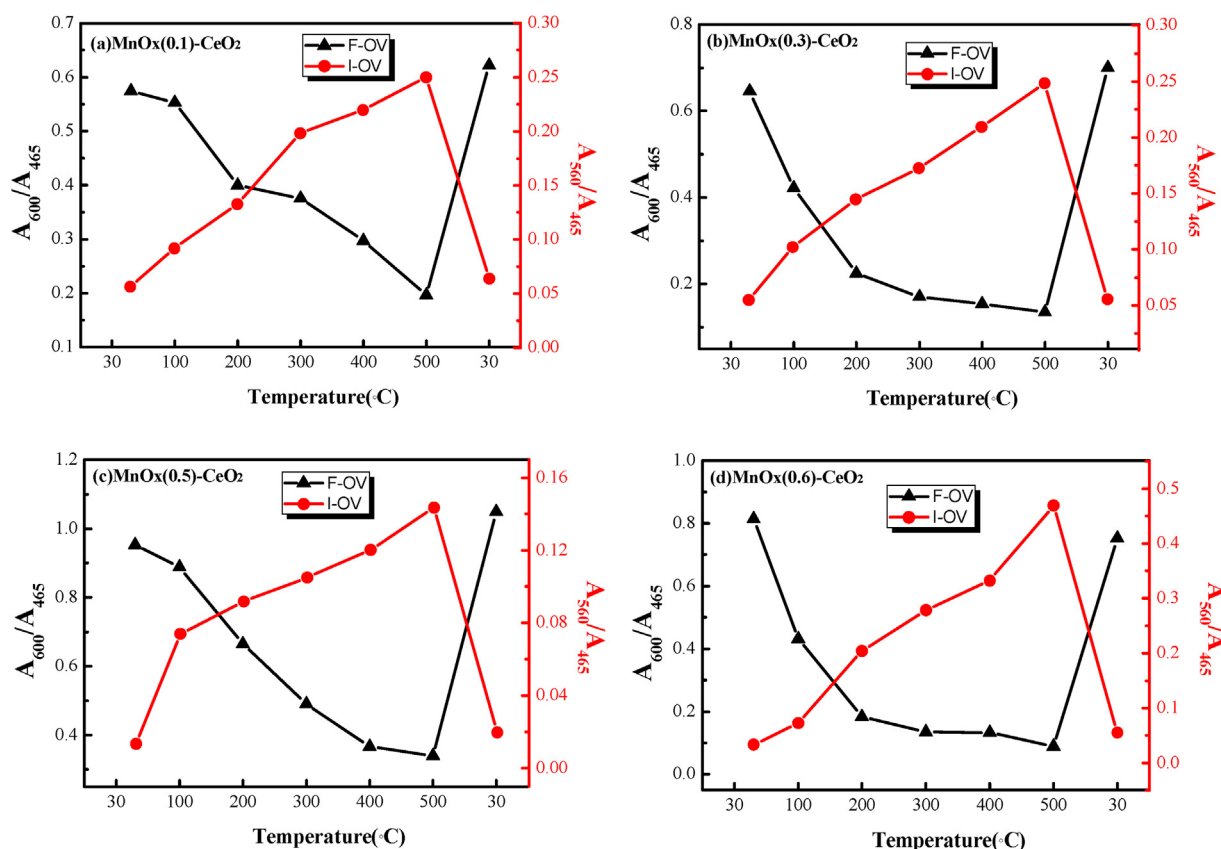
Fig. 12. Peak intensity ratios of A_{560}/A_{465} and A_{600}/A_{465} from spectra of (a)MnOx(0.1)-CeO$_2$, (b)MnOx(0.3)-CeO$_2$, (c)MnOx(0.5)-CeO$_2$ and (d)MnOx(0.6)-CeO$_2$ under reactants (soot and 10%O$_2$/Ar). The peak intensity values were taken from Fig. 11.

loss and supplement of oxygen, respectively. The rapid generation of O-vacancies in CeO$_2$ that can improve its oxygen storage capacity (OSC) makes it a promising material for catalysis. Considering all these studies, we deduce that during soot oxidation, surface oxygen of catalyst escape to the gas phase to participate in the reaction, forming O-vacancies in the lattice. And by adsorbing gas O$_2$ during cooling process, the O-vacancies are refilled. This deduction can accurately correspond to the observation in Fig. 9(f), where the intensity of 560 cm^{-1} band increases with rising temperature and recovers along with the decreasing temperature. Other than these defect bands, a new Raman band at around 1600 cm^{-1} is assigned to soot particles. The band gradually decreases during temperature range of 200–300 °C, in good agreement with the TPO result where combustion and consumption of soot over MnO$_x$(0.4)-CeO$_2$ catalysts begin during 200–300 °C.

The intensity ratios are listed in Fig. 10, where A_{465}, A_{560}, and A_{600} correspond to the maximum intensity of F$_{2g}$, I—OV, and F—OV, respectively (more details in S1–S4). Fig. 10(a,b) reveals that, for CeO$_2$ and MnO$_x$(0.4)-CeO$_2$, on one hand, relative intensity of F—OV systematically decreases in the heating process following an increase in the cooling process; on the other hand, when soot is added in the system, the changing trend is more evident. Therefore, based on above observations, a plausible explanation is proposed: during the heating process, interstitial oxygen readily escape from the lattice, resulting in the elimination of F—OV; and in the cooling process, interstitial oxygen are replenished by lattice oxygen or gas O$_2$, explaining the recovery trend of F—OV. Then in the case of soot being included in the system, it appears that the reactant soot can further induces the redox cycle, enhancing the mobility of oxygen. Moreover, when comparing the ratio of A_{600}/A_{465} between CeO$_2$ and MnO$_x$(0.4)-CeO$_2$ in Fig. 10(c), we notice that the latter one has higher O-vacancy concentration at starting temperature

30 °C, owing mainly to the incorporating of Mn ions. Indeed, the incorporation can enhances the formation of O-vacancies by forming Mn—O—Ce bonds and interacting with adjacent O, leaving more F—OV in the crystal due to a charge compensation mechanism. Also note that the decreasing trend of MnO$_x$(0.4)-CeO$_2$ is more obvious than CeO$_2$, showing that the O atoms in Mn-incorporated ceria are highly mobile during heating and reaction. In fact, that is the essential reason for MnO$_x$(0.4)-CeO$_2$ to have excellent redox property, high oxygen storage capacity and enhanced catalyst activity.

For MnO$_x$(0.4)-CeO$_2$, as we compare two ratios of A_{560}/A_{465} and A_{600}/A_{465}, an interesting pattern is shown in Fig. 10(d). It clearly shows a direct correlation between the I—OV and F—OV. The value of A_{600}/A_{465} increases at first and decreases subsequently as we observed before. However, for A_{560}/A_{465}, its variation trend is exactly contrary. Obviously, transform relation exists between I—OV and F—OV. To reinforce the above opinion, in situ UV Raman under reactants (soot and 10%O$_2$/Ar) for all other samples had been done (Figs. 11 and 12). And the transform relation between I—OV and F—OV can be found in all samples (more details in S5–S8). Thus, based on this observation and XPS result, we figure that during the reaction process, interstitial oxygen atoms adjacent to Mn^{4+} ions are the first to escape from the bulk crystal, along with Mn^{4+} being reduced to Mn^{3+}; meanwhile, the original F—OV are converted into I—OV, functioning as the absorbed sites for active oxygen species and key segment for activating gas O$_2$ into active species. This can well explain the enhanced catalyst activity of MnO$_x$(0.4)-CeO$_2$ for soot combustion.

Then for lattice phase study, we use visible Raman as an excitation source. In situ visible Raman spectra of MnO$_x$ and MnO$_x$(0.4)-CeO$_2$ were recorded under Ar, 10%O$_2$/Ar and reactants in a temperature range of 30–500 °C. For MnO$_x$ in Fig. 13(a–c), it may exists in the form of R-MnO$_2$, β-MnO$_2$ and α-Mn$_2$O$_3$, mainly
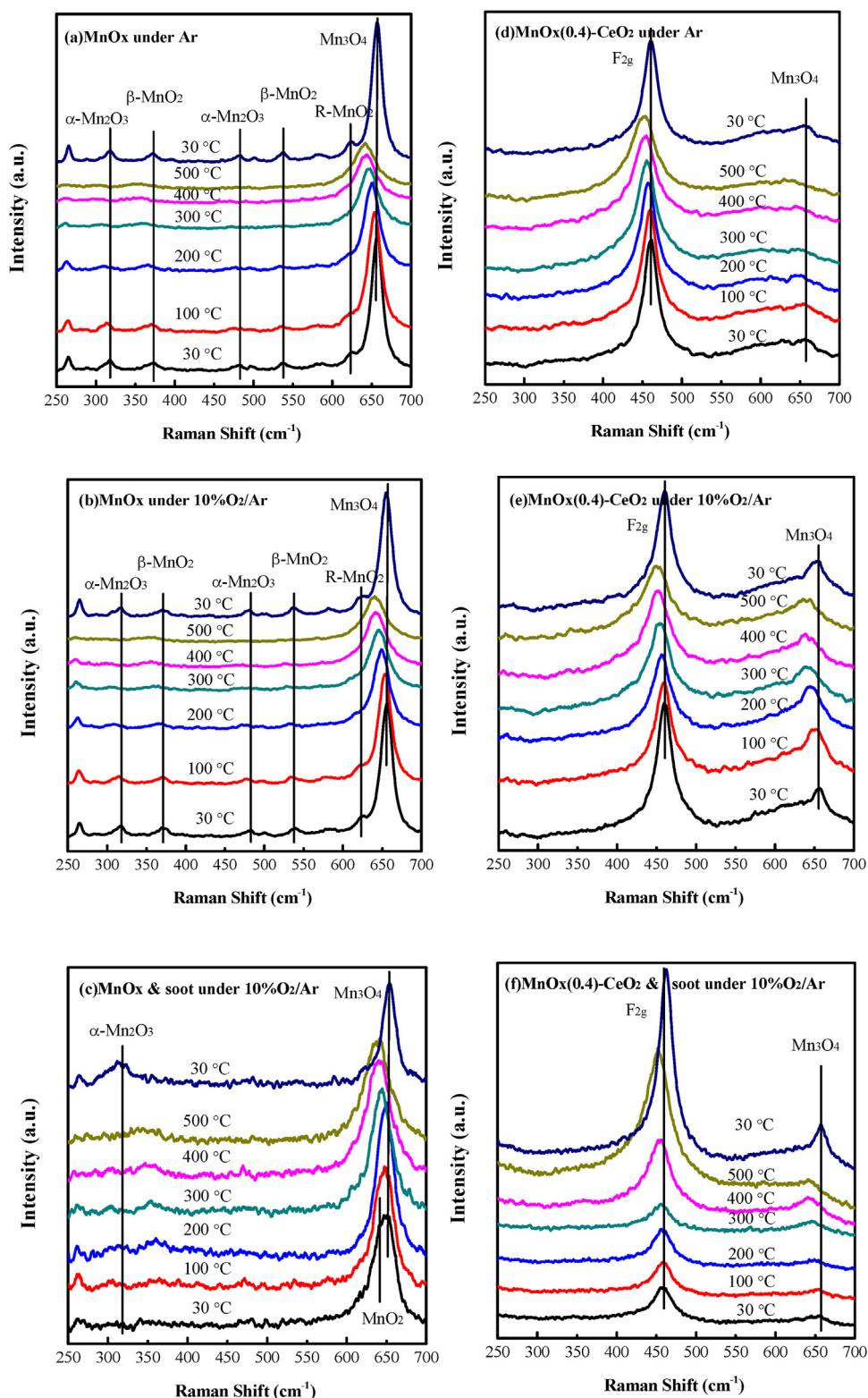
Fig. 13. In situ visible Raman spectra of (a,b,c) MnO$_x$ and (d,e,f) MnO$_x$(0.4)-CeO$_2$ under (a,d) Ar, (b,e) 10%O$_2$/Ar and (c,f) reactants (soot and 10%O$_2$/Ar). Temperature programme: ramping rate of 10 °C min^{-1} from 30 to 500 °C and 20 °C min^{-1} from 500 to 30 °C.

of Mn$_3$O$_4$. Under atmosphere of Ar and 10%O$_2$/Ar, it appears that the week bands associated with R-MnO$_2$, β-MnO$_2$ and α-Mn$_2$O$_3$ recover from downtrend in the cooling process. However, when the reactant is added, the R-MnO$_2$ band disappears along with appearance of a distinct band of α-Mn$_2$O$_3$ around 315 cm^{-1}, proving that irreversible phase change occurs during reaction. As for MnO$_x$(0.4)-

CeO$_2$ (Fig. 13d–f), the visible Raman spectra are dominated by the strong F$_{2g}$ mode of the CeO$_2$ fluorite phase at 465 cm^{-1}, together with weak band associated with Mn$_3$O$_4$ at 655 cm^{-1}. There are no obvious change of Mn$_3$O$_4$ band and also no other lattice phases to give new bands in the spectra under reactant during the heating and cooling process, evidence for no irreversible phase change in
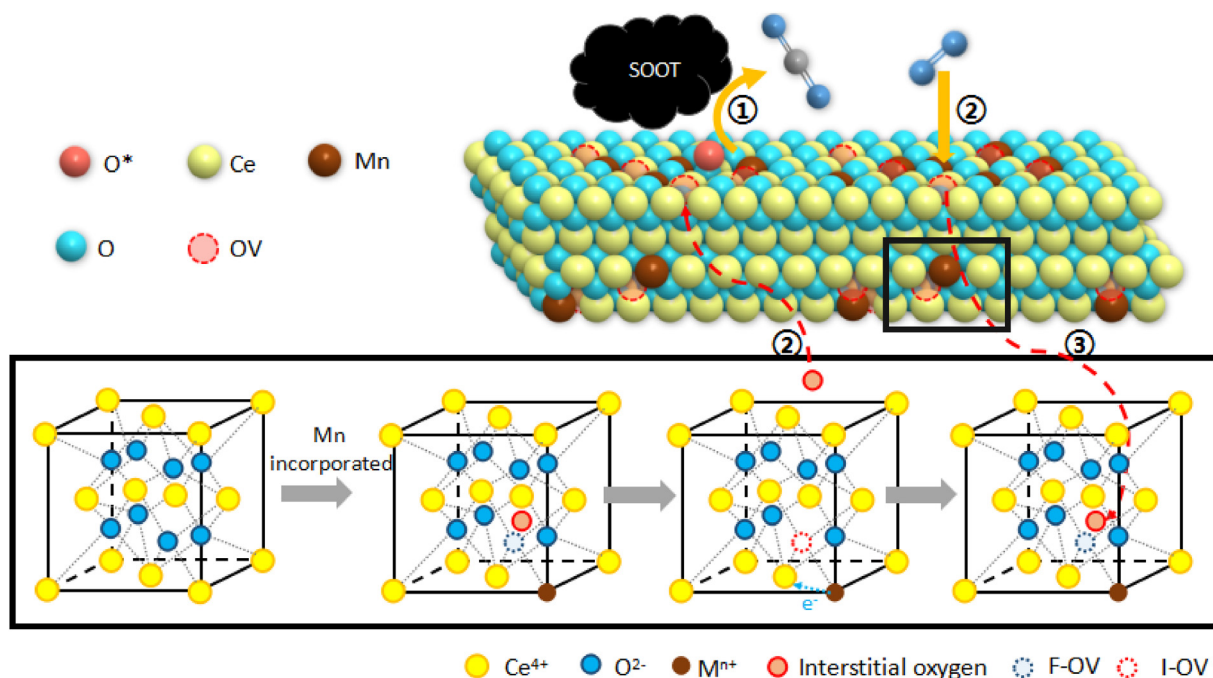
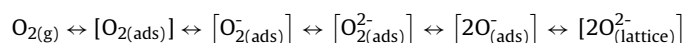**Scheme 1.** Evolution of oxygen vacancies in soot catalytic oxidation.

these solid solution. This is in clear contrast to the phase changes as observed in Raman for the MnO_x. Therefore, compared to the MnO_x, reduced Mn ions in $MnO_x(0.4)$-CeO_2 are easier to be oxidized to highly charged ions, mostly due to the active electron transfer between Mn^{3+} and Ce^{4+}.

To sum up, the enhanced redox properties of $MnO_x(0.4)$-CeO_2 are mainly because of the higher concentration of F—OV compared to pure CeO_2, resulting from incorporating Mn into the CeO_2 lattice which makes the interstitial oxygen highly mobilized and can actively escape from lattice to participate in the soot oxidation. And it is important to note that there is certain transform relation between F—OV and I—OV, namely, the interstitial oxygen adjacent to Mn^{4+} can easily escape to the gas phase, meanwhile, Mn^{4+} is reduced to low valence, leaving the origin F—OV to transform into I—OV. Moreover, I—OV function as the absorbed sites for active oxygen species and key segment for activating gas O_2 into active species. When comparing to MnO_x, it is found that reduced Mn ions in $MnO_x(0.4)$-CeO_2 are easier to be oxidized to highly charged ions, mostly due to the active electron transfer between Mn^{3+} and Ce^{4+}, which is the crucial part in redox cycle.
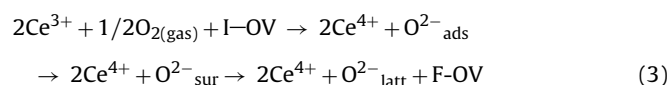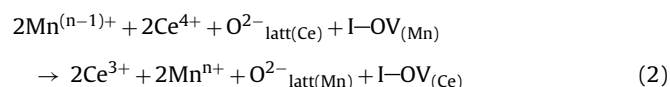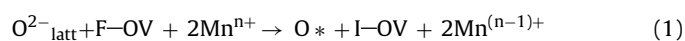
3.5. Evolution of oxygen vacancies in soot catalytic oxidation

After years of investigations, numerous studies regarding to ceria-based oxides for soot oxidation had been published. It had been reported that the ceria-based catalyst was operative via an oxidation-reduction cycle [23,24]. As is widely accepted that reaction mechanism includes the formation of superoxides, peroxides, O-vacancies, spill-over procedure and re-oxidation process [23,46,58,59], which is concisely illustrated in Scheme 1. (i)When soot is introduced into the system, substoichiometric ceria-based oxides is produced upon oxygen elimination from the oxide surface through spill-over procedure and the subsequent formation of O-vacancies [58,59]. The escaped active oxygen is then participate in the soot oxidation. (ii)Surface O-vacancies are then quickly filled by the gas phase or subsurface oxygen [59]. (iii)The alter-

nating reduction-oxidation process may proceed according to the following scheme [23,60]:

$$O_{2(g)} \leftrightarrow [O_{2(ads)}] \leftrightarrow [O^-_{2(ads)}] \leftrightarrow [O^{2-}_{2(ads)}] \leftrightarrow [2O^-_{(ads)}] \leftrightarrow [2O^{2-}_{(lattice)}]$$

However, the nature of the active oxygen species and its relationship with O-vacancies, especially the evolution of O-vacancies, are still not well-known. Here we propose the evolution of O-vacancies taking into account the Raman and XPS results, which is concisely illustrated in Scheme 1. It is notable that we address the roles of two types of O-vacancies (F—OV and I—OV) and find out the transform relation between them. In the proposed evolution process, (1)Mn incorporates into the CeO_2 lattice, replacing Ce ion from its original site, thus causing relocation of adjacent oxygen anion from its lattice position to an interstitial position and leaving a vacancy behind. (Here, as for F—OV, we only illustrate the case created by Mn-incorporation.) The relocated oxygen is referred as interstitial oxygen (O^{2-}_{latt}). Then Mn^{n+} is easily reduced to $Mn^{(n-1)+}$ via gaining an electron from interstitial oxygen. Due to the loss of electron, the unstable interstitial oxygen is highly mobilized, resulting in its escape form the lattice and becoming an active oxygen (O^*). Meanwhile, F—OV transforms to I—OV. (2)Then Ce^{4+} captures one electron from $Mn^{(n-1)+}$, leading to formations of Ce^{3+} and Mn^{n+}. (3) Finally, gas phase O_2 molecules ($O_{2(gas)}$) act as oxygen storage cavern to supplement the consumed active oxygen ($O_2 \leftrightarrow O_{ads} \leftrightarrow O_{sur} \leftrightarrow O_{latt}$) and guarantee the metal ions reduction-oxidation reaction cycle [23]. And Ce^{3+} is subsequently oxidized to Ce^{4+}, back to the original chemical state.

$$O^{2-}_{latt} + F—OV + 2Mn^{n+} \rightarrow O* + I—OV + 2Mn^{(n-1)+} \tag{1}$$

$$2Mn^{(n-1)+} + 2Ce^{4+} + O^{2-}_{latt(Ce)} + I—OV_{(Mn)}$$
$$\rightarrow 2Ce^{3+} + 2Mn^{n+} + O^{2-}_{latt(Mn)} + I—OV_{(Ce)} \tag{2}$$

$$2Ce^{3+} + 1/2O_{2(gas)} + I—OV \rightarrow 2Ce^{4+} + O^{2-}_{ads}$$
$$\rightarrow 2Ce^{4+} + O^{2-}_{sur} \rightarrow 2Ce^{4+} + O^{2-}_{latt} + F—OV \tag{3}$$

4. Conclusions

For the insights into the O-vacancies, a series of MnOx(z)-CeO$_2$ catalysts with various Mn/(Mn + Ce) molar ratios were investigated. It was found that the Mn-incorporating content can obviously affect the formation of Mn—Ce solid solution and subsequently determine the physicochemical and catalytic properties of the catalyst. Especially, MnO$_x$(0.4)-CeO$_2$ exhibited the highest catalytic activity. Moderate Mn-incorporating amount favored to the formation of O-vacancies, and then the redox properties of the catalyst were enhanced. Therefore, the mobility and transformation of oxygen species on the catalyst were improved, which highly promoted the catalytic oxidation of soot. In addition, the active species including Mn^{4+}/Mn^{3+}(Mn^{2+}), O$_{latt}$, O$_{sur}$ and Ce^{4+}/Ce^{3+} were considered to play important roles in soot oxidation. Furthermore, as for O-vacancy, F—OV and I—OV were clarified via in situ UV Raman. F—OV band, which is cause by the relocation of lattice oxygen form tetrahedral sites to the octahedral sites, is located at 600 cm^{-1}. I—OV band, the intrinsic defect, is located at 560 cm^{-1}. The transform relation between F—OV and I—OV were found. Thus, the evolution of these two types of O-vacancies during soot oxidation is elaborated, which is a significant part of understanding catalytic oxidation.

Acknowledgements

Appendix A. Supplementary data

Supplementary data associated with this article can be found, in the online version, at http://dx.doi.org/10.1016/j.apcatb.2017.06.071.

References

[1] L. Pahalagedara, H. Sharma, C. Kuo, S. Dharmarathna, A. Joshi, S.L. Suib, A.B. Mhadeshwar, Energy Fuel 26 (2012) 6757–6764.
[2] Y. Sekine, H. Koyama, M. Matsukata, E. Kikuchi, Fuel 103 (2013) 2–6.
[3] S. Liu, X. Wu, D. Weng, M. Li, H. Lee, J. Chem. Eng. 203 (2012) 25–35.
[4] P.A. Kumar, M.D. Tanwar, S. Bensaid, N. Russo, D. Fino, Chem. Eng. J. 207-208 (2012) 258–266.
[5] N. Russo, D. Fino, G. Saracco, V. Specchia, Catal. Today 137 (2008) 306–311.
[6] M. Dhakad, T. Mitsuhashi, S. Rayalu, P. Doggali, S. Bakardjiva, J. Subrt, D. Fino, H. Haneda, N. Labhsetwar, Catal. Today 132 (2008) 188–193.
[7] K. Shimizu, H. Kawachi, A. Satsuma, Appl. Catal. B: Environ. 96 (2010) 169–175.
[8] X. Li, S. Wei, Z. Zhang, Y. Zhang, Z. Wang, Q. Su, X. Gao, Catal. Today 175 (2011) 112–116.
[9] Q. Shen, G. Lu, C. Du, Y. Guo, Y. Wang, Y. Guo, X. Gong, J. Chem. Eng. 218 (2013) 164–172.
[10] E. Aneggi, C. de Leitenburg, G. Dolcetti, A. Trovarelli, Catal. Today 114 (2006) 40–47.
[11] A. Vasile, V. Bratan, C. Hornoiu, M. Caldararu, N.I. Ionescu, T. Yuzhakova, Á. Rédey, Appl. Catal. B: Environ. 140-141 (2013) 25–31.
[12] M.V. Ganduglia-Pirovano, A. Hofmann, J. Sauer, Surf. Sci. Rep. 62 (2007) 219–270.
[13] M.E. Becerra, N.P. Arias, O.H. Giraldo, F.E. López Suárez, M.J. Illán Gómez, A. Bueno López, Appl. Catal. B: Environ. 102 (2011) 260–266.
[14] S.S.T. Bastos, J.J.M. Órfão, M.M.A. Freitas, M.F.R. Pereira, J.L. Figueiredo, Appl. Catal. B: Environ. 93 (2009) 30–37.
[15] V.P. Santos, M.F.R. Pereira, J.J.M. Órfão, J.L. Figueiredo, Appl. Catal. B: Environ. 99 (2010) 353–363.
[16] M.A. Peluso, E. Pronsato, J.E. Sambeth, H.J. Thomas, G. Busca, Appl. Catal. B: Environ. 78 (2008) 73–79.
[17] X. Wu, S. Liu, D. Weng, F. Lin, R. Ran, J. Hazard. Mater. 187 (2011) 283–290.
[18] Q. Liang, X. Wu, D. Weng, H. Xu, Catal. Today 139 (2008) 113–118.
[19] I. Spassova, T. Tsontcheva, N. Velichkova, M. Khristova, D. Nihtianova, J. Colloid Interf. Sci. 374 (2012) 267–277.
[20] H. Jiang, Q. Xu, J. Mater. Chem. (2011) 13705–13725.
[21] A. Setiabudi, J. Chen, G. Mul, M. Makkee, J.A. Moulijn, Appl. Catal. B: Environ. 51 (2004) 9–19.
[22] W. Shan, N. Ma, J. Yang, X. Dong, C. Liu, L. Wei, J. Nat. Gas Chem. 19 (2010) 86–90.
[23] M. Machida, Y. Murata, K. Kishikawa, D. Zhang, K. Ikeue, Chem. Mater. 20 (2008) 4489–4494.
[24] N. Guillén-Hurtado, A. García-García, A. Bueno-López, J. Catal. 299 (2013) 181–187.
[25] Z. Wu, M. Li, J. Howe, H.M. Meyer, S.H. Overbury, Langmuir 26 (2010) 16595–16606.
[26] S. Agarwal, X. Zhu, E.J.M. Hensen, L. Lefferts, B.L. Mojet, J. Phys. Chem. C 118 (2014) 4131–4142.
[27] M. Fu, K. Wang, R. Yu, X. Wen, M. Zhang, B. Huang, J. Wu, D. Ye, H. Liang, Chin. J. Inorg. Chem. 28 (2012) 1593–1600.
[28] M. Zhang, M. Fu, J. Wu, B. Huang, H. Liang, D. Ye, J. Chin. Soc. Rare Earths 29 (2011) 303–309.
[29] M. Fu, X. Yue, D. Ye, J. Ouyang, B. Huang, J. Wu, H. Liang, Catal. Today 153 (2010) 125–132.
[30] X. Wu, F. Lin, H. Xu, D. Weng, Appl. Catal. B: Environ. 96 (2010) 101–109.
[31] T. Sato, T. Komanoya, Catal. Commun. 10 (2009) 1095–1098.
[32] P. Borker, A.V. Salker, Mater. Chem. Phys. 103 (2007) 366–370.
[33] K. Tikhomirov, O. Kröcher, M. Elsener, A. Wokaun, Appl. Catal. B: Environ. 64 (2006) 72–78.
[34] X. Wu, S. Liu, D. Weng, F. Lin, Catal. Commun. 12 (2011) 345–348.
[35] R. Zhang, A. Villanueva, H. Alamdari, S. Kaliaguine, J. Mol. Catal. A: Chem. 258 (2006) 22–34.
[36] S. Kaliaguine, A. Van Neste, V. Szabo, J.E. Gallot, M. Bassir, R. Muzychuk, Appl. Catal. A: Gen. 209 (2001) 345–358.
[37] M. Machida, M. Uto, D. Kurogi, T. Kijima, Chem. Mater. 12 (2000) 3158–3164.
[38] K. Krishna, A. Bueno-López, M. Makkee, J.A. Moulijn, Appl. Catal. B: Environ. 75 (2007) 189–200.
[39] H. Muroyama, S. Hano, T. Matsui, K. Eguchi, Catal. Today 153 (2010) 133–135.
[40] P. Venkataswamy, K.N. Rao, D. Jampaiah, B.M. Reddy, Appl. Catal. B: Environ. 162 (2015) 122–132.
[41] Y. Zhang, L. Zhang, J. Deng, H. Dai, H. He, Inorg. Chem. 48 (2009) 2181–2192.
[42] Y. Li, Q. Sun, M. Kong, W. Shi, J. Huang, J. Tang, X. Zhao, J. Phys. Chem. C 115 (2011) 14050–14057.
[43] H. Li, G. Qi, X. Tana, X. Zhang, W. Huang, W. Li, W. Shen, Appl. Catal. B: Environ. 103 (2011) 54–61.
[44] H. Li, G. Lu, Q. Dai, Y. Wang, Y. Guo, Y. Guo, Appl. Catal. B: Environ. 102 (2011) 475–483.
[45] X. Wang, Q. Kang, D. Li, Appl. Catal. B: Environ. 86 (2009) 166–175.
[46] V. Rico-Pérez, E. Aneggi, A. Bueno-López, A. Trovarelli, Appl. Catal. B: Environ. 197 (2016) 95–104.
[47] M. Piumetti, S. Bensaid, N. Russo, D. Fino, Appl. Catal. B: Environ. 180 (2016) 271–282.
[48] K. An, G.A. Somorjai, Catal. Lett. 145 (2015) 233–248.
[49] J.C. Védrine, Appl. Catal. A: Gen. 474 (2014) 40–50.
[50] T. Taniguchi, T. Watanabe, N. Sugiyama, A.K. Subramani, H. Wagata, N. Matsushita, M. Yoshimura, J. Phys. Chem. C 113 (2009) 19789–19793.
[51] M. Luo, Z. Yan, L. Jin, M. He, J. Phys. Chem. B 110 (2006) 13068–13071.
[52] J. Xu, P. Li, X. Song, C. He, J. Yu, Y. Han, J. Phys. Chem. Lett. (2010) 1648–1654.
[53] T.X. Sayle, M. Molinari, S. Das, U.M. Bhatta, G. Mobus, S.C. Parker, S. Seal, D.C. Sayle, Nanoscale 5 (2013) 6063–6073.
[54] A. Walsh, S.M. Woodley, C.R.A. Catlow, A.A. Sokol, Solid State Ion. 184 (2011) 52–56.
[55] L. Minervini, M. Zacate, R. Grimes, Solid State Ion. 116 (1999) 339–349.
[56] A. Nakajima, A. Yoshihara, M. Ishigame, Phys. Rev. B 50 (1994) 13297–13307.
[57] D. Ye, D. Gao, G. Yu, X. Shen, F. Gu, J. Hazard Mater. 127 (2005) 149–155.
[58] M.S. Gross, M.A. Ulla, C.A. Querini, J. Mol. Catal. A: Chem. 352 (2012) 86–94.
[59] M.S. Gross, B.S. Sánchez, C.A. Querini, J. Chem. Eng. 168 (2011) 413–419.
[60] C. Binet, M. Daturi, J.C. Lavalley, Catal. Today 50 (1999) 207–225.